Journal of Materials Science: Materials in Medicine (2018) 29:145
https://doi.org/10.1007/s10856-018-6153-2

BIOMATERIALS SYNTHESIS AND CHARACTERIZATION

Original Research

Surface topography of polylactic acid nanofibrous mats: influence on blood compatibility

Abiramy Soundararajan[1] · Jyorthana Muralidhar R.[1] · Ramya Dhandapani[1] · Janani Radhakrishnan[1] · Amrutha Manigandan[1] · Sivashankari Kalyanasundaram[1] · Swaminathan Sethuraman[1] · Anuradha Subramanian[1]

Received: 15 March 2018 / Accepted: 18 August 2018 / Published online: 29 August 2018

Abstract

Fabricating nanofibrous scaffolds with robust blood compatibility remains an unmet challenge for cardiovascular applications since anti-thrombogenic surface coatings did not withstand physiological shear force. Hence, the present study envisages the influence of smooth and porous topographies of poly(lactic acid) (PLA) nanofibers on hemocompatibility as it could offer time-independent blood compatibility. Further, recent studies have evolved to integrate various contrasting agents for augmenting the prognostic properties of tissue engineered scaffolds; an attempt was also made to synthesize Curcumin–superparamagnetic iron oxide nanoparticle complex (Cur–SPION) as a contrasting agent and impregnated into PLA nanofibers for evaluating the blood compatibility. Herein, electrospun nanofibers of PLA with different topographies (smooth and porous) were fabricated and characterized for surface morphology, zeta potential, fluorescence, and crystallinity. The scaffolds with smooth, porous and rough surface topographies were thoroughly investigated for its hemocompatibility by evaluating hemolysis percentage, platelet adhesion, in vitro kinetic clotting time, serum protein adsorption, plasma recalcification time (PRT), capture and release of erythrocytes. Although the nanofibers of all three groups showed acceptable hemolytic percentage (HP < 5%), the adhered RBCs on Cur–SPION based fibers undergo morphological transformation from biconcave discocytes to echinocytes with cube-like protrusions. On the contrary, no morphological changes were observed in RBCs cultured on smooth and porous nanofibers. Porous fibers exhibited excellent anti-thrombogenic property and adhered lesser platelets and maintained the discoidal morphology of native platelets. Cur–SPION integrated PLA nanofibers showed inactivated platelets with anti-thrombogenic activity compared to smooth nanofibers. In conclusion, PLA nanofibers porous topography did not affect the RBC membrane integrity and maintained discoidal morphology of platelets with superior anti-thrombogenic activity. However, smooth and Cur–SPION integrated PLA nanofibers were found to activate the platelets and deform the RBC membrane integrity, respectively. Hence, the nanofibers with porous structures provide an ideal topography for time-independent hemocompatibility.

✉ Anuradha Subramanian
anuradha@bioengg.sastra.edu

[1] Centre for Nanotechnology & Advanced Biomaterials, School of Chemical & Biotechnology, SASTRA Deemed University, Thanjavur 613 401, India

Graphical Abstract

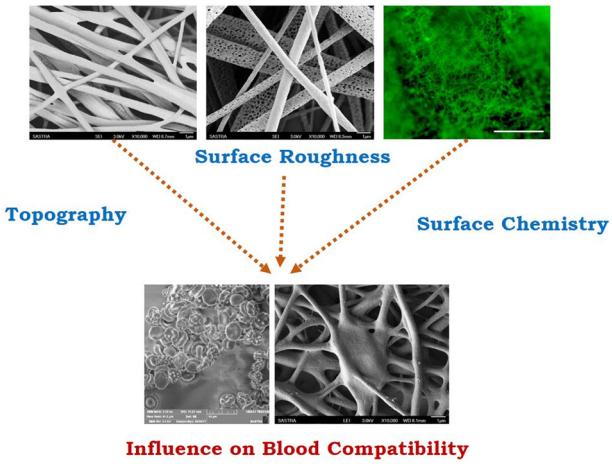

1 Background

Cardiovascular disease is the leading cause of worldwide mortality that is accounting for 31% of all global deaths. The annual incidence of cardiovascular disease-related mortalities is expected to rise from 17.3 million in 2013 to 23.6 million worldwide by 2030 [1]. Each year more than 1.4 million people need arterial prostheses but follow-up studies have shown unacceptable failures of vascular grafts due to the adverse blood–material interactions like thrombogenicity, which is an inherent characteristic of most synthetic graft surfaces [2]. When blood contacts foreign biomaterial surface directly, sequential deleterious effects such as competitive adsorption of plasma proteins, recruitment, degranulation and platelet aggregation leads to platelet plug formation. The activation of coagulation factors following the platelets aggregation ultimately results in thrombus or blood clot [3]. Surface wettability and surface topography are crucial parameters responsible for Vroman-effect [4]. Plasma protein adsorption increases with increasing surface wettability and promotes undesirable thrombolytic events. Further, shear stress experienced by the cells is directly proportional to surface roughness of the material, which in turn increases hemolysis [5]. Hence, many attempts have been made to control the protein and platelet adsorption via various surface modifying strategies, thereby improve hemocompatibility and anticoagulant properties of synthetic grafts [6].

Electrospun scaffolds have been extensively used for vascular tissue regeneration, as it resembles the native three-dimensional network of extracellular matrix in addition to the combination of a higher surface area-to-volume ratio. The microporous structures of electrospun scaffolds facilitate adhesion, migration, proliferation, and differentiation of cells [7, 8]. Electrospinning is a versatile technique that would tailor the mechanical and biological properties apart from tuning the fiber dimension and its orientation [9, 10]. To enhance the hemocompatibility, surface of the electrospun scaffolds has been modified either by coating of anti-thrombogenic factors, bio-inert and inorganic coatings or by creating endothelial cell friendly surfaces using plasma treatment and wet chemical modification [11]. Surface chemistry of fabricated nanomaterials also induces significant changes in the nano-bio interface due to selective binding of cells with active functional groups on biomaterials surface [12, 13]. However, a coating of anticoagulants or any organic and inorganic coatings provide transient hemocompatibility, which gradually ceases over time. Similarly, establishing cell-friendly surfaces would promote the attachment of cells, platelets rather than exhibiting specificity towards endothelial attachment [14]. Like surface chemistry, the surface topography of electrospun scaffolds influences the protein adsorption, modulates focal adhesion patterns with stress fiber orientation and regulates the transcriptional activity of cells thereby mediating cell adhesion, cell spreading and cell phenotype, respectively [15]. Hence, electrospun nanofibers with different topographies may be an alternate approach to enhance the blood compatibility of scaffolds due to time-independent activity. So far, topographical features of electrospun scaffolds have not been evaluated for hemocompatibility.

On the other hand, fabrication of electrospun scaffolds with diagnostic potential is also emerging to aid simultaneous imaging of scaffold performance in vivo using non-invasive techniques such as magnetic resonance imaging (MRI), optical imaging using fluorescence, and luminescence characteristics. Among the various preclinical and

clinical imaging strategies, MRI has been the preferred modality to assess anatomical and functional features due to its non-invasiveness, higher penetration strength, and safety [16]. Scaffolds have been directly or indirectly imaged using integrated magnetic materials or magnetically labeled cells to determine cellular information, respectively [17]. Iron oxide nanoparticles embedded composite nanofibers have gained attention as a diagnostic mat with enhanced negative contrast in MRI [18]. Although MRI based monitoring of scaffold is considered safe compared to Computed Tomography, the lesser sensitivity of MRI limits its potential application. Therefore, to enhance the sensitivity and spatial resolution, MRI has been integrated with other imaging modalities such as PET, X-ray and optical imaging to attain the complementary advantages of both the techniques [19]. Recently, fluorescence based optical imaging of electrospun fibers using curcumin has been reported for tissue engineering applications [20–22]. However, no studies have reported the influence of such surface modifications of tissue scaffolds on blood–material interactions. Hence, the present study aims to understand the role of surface topography and surface chemistry on hemocompatibility by comparing porous, smooth and Cur–SPION impregnated PLA nanofibers.

PLA has been widely reported polymer for vascular applications due to its known biodegradable, biocompatible with high tensile and elongation properties. Hence in this study, PLA nanofibers were fabricated with smooth and porous topographies and fibers were developed with Cur–SPION that would impart fluorescence and magnetic contrasting characteristics to the scaffolds. Fluorescent property of the as-spun fibers was confirmed using a fluorescent microscope. Hemocompatibility of various surfaces such as smooth, porous and curcumin–SPION impregnated nanofibers were determined by evaluating hemolysis percentage, platelet adhesion, capture and release of erythrocytes, in vitro kinetic clotting time, plasma recalcification time (PRT) and electrophoretic separation of adsorbed serum protein.

2 Materials and methods

2.1 Materials

Poly(L-lactic acid) (M_w: 69,000 g/mol) was procured from Lakeshore Biomaterials, Birmingham, USA. Chemicals such as iron (III) chloride hexahydrate ($FeCl_3{\cdot}6H_2O$), iron (II) chloride tetrahydrate ($FeCl_2{\cdot}4H_2O$), isopropyl alcohol (IPA), dichloromethane (DCM), acetone, and N, N-dimethylformamide (DMF) were purchased from Merck, India. Curcumin, extracted from *Curcuma longa*, was procured from Sigma Aldrich, India. Ethanol and all the other chemicals were used without any further purification.

2.2 Fabrication of smooth and porous nanofibers

PLA nanofibers with porous topography were fabricated using 7% (w/v) PLA in DCM/acetone of 7:3 ratio by electrospinning. Polymer solution was fed into a glass syringe with 24 G needle and fixed in a syringe pump (KD Scientific 200, USA) to control flow rate at 0.004 mL/min. The needle tip and collector were maintained at a distance of 12 cm and a high voltage of 25 kV was applied. PLA nanofibers of smooth topography were developed by using DMF instead of acetone in the co-solvent system while keeping other parameters such as concentration, applied voltage, needle gauge, tip–target distance and flow rate same as mentioned for porous nanofibers. Electrospun nanofibers were stored under vacuum at room temperature until further characterizations.

2.3 Cur–SPION embedded PLA nanofibers

Hydrophobic SPION were synthesized by co-precipitation method [23]. In brief, an equimolar concentration of $FeCl_3{\cdot}6H_2O$ and $FeCl_2{\cdot}4H_2O$ dissolved in double distilled water was heated up to 80 °C under magnetic stirring. On adding 1.5 mL ammonia, the solution turns black followed with the addition of 450 µL oleic acid (capping agent) and maintained for 1 h at 90 °C. Nanoparticles magnetically separated were washed with alternate cycles of IPA and acetone. The Cur–SPION complex was formed by ultrasonication of SPION and curcumin in equal weight ratio for 10 min. The prepared complex was washed several times using deionized water by magnetic decantation and further freeze-dried to obtain Cur–SPION. Five mg/mL of developed Cur–SPION was dispersed in PLA polymeric solution (DCM/DMF as co-solvent) to fabricate curcumin loaded magnetic electrospun nanofibers by maintaining the operating parameters constant as mentioned for smooth fiber fabrication.

2.4 Physio-chemical characterization of Cur–SPION

Hydrodynamic diameter and surface charge of synthesized nanoparticles (SPION and Cur–SPION) were determined using dynamic light scattering (Zetasizer Nano ZS-90, Malvern Instruments Ltd, UK) at 25 °C. Samples dispersed in double distilled water were subjected to sonication for 5 min prior analysis. Data are represented as mean ± standard deviation from triplicates of each sample. Crystallinity of SPION and Cur–SPION was studied using X-ray diffractometer (XRD) (D8 Focus, Bruker, Germany) with Cu-Kα radiation of wavelength 1.5418 Å. Diffraction pattern was examined for 2θ values from 10° to 80° with a step size of 0.01°/min.

2.5 Surface morphology

The morphology of nanoparticles (SPION and Cur–SPION) and smooth, porous and Cur–SPION-embedded nanofibers were observed using field emission–scanning electron microscope (SEM, JEOL FE-SEM 6701F, Japan) at 3 kV accelerating voltage. These scaffolds were gold coated using an auto sputter fine coater (JFC 1600, JEOL, Japan) before imaging. Average diameter of nanoparticles and nanofibers were determined by measuring the diameter of hundred individual particles or fibers.

2.6 Fluorescence Imaging

The auto-fluorescence of curcumin complex in Cur–SPION and Cur–SPION loaded PLA smooth nanofibers were confirmed using fluorescence microscopy (ZEISS, Scope A1, USA). A drop of nanoparticles well dispersed in deionized water was placed on a microscopic slide and covered with the coverslip for imaging.

2.7 Contact angle measurements

Static contact angle (θ) measurements of electrospun smooth, rough and porous nanofibrous scaffolds were estimated using goniometer (Rame-Hart Instrument 250-F1 with DROP image Advance v2.3, USA) to evaluate the wettable property of nanofibrous scaffolds. Droplets of deionized water were carefully placed onto the sample surface ($n = 6$) to acquire images and water contact angle was recorded.

2.8 Hemocompatibility studies

2.8.1 Hemolysis

The red blood cell (RBC) membrane integrity on exposure to various topographies of nanofibers was examined by hemolysis assay. Briefly, blood from healthy adult volunteer was drawn in 0.5 mL of 0.1 M ethylenediamine tetracetic acid (EDTA) to avoid coagulation. The solution was centrifuged at 1500 rpm for 15 min to obtain packed RBCs. The pellet was washed with PBS (pH 7.4) thrice and finally, the volume was made up to 3.5 mL with PBS. In a fresh tube, 0.2 mL of diluted suspension was transferred and mixed with 0.8 mL of deionized water (as positive control) or PBS (as negative control). Samples were exposed to 0.2 mL of diluted RBC suspension and incubated at 37 °C for 2 h, followed by centrifugation at 1500 rpm for 15 min. The haemoglobin released in plasma was calculated by recording the absorbance of the supernatant at 540nm [24, 25]. The hemolysis percentage (HP) was calculated using the following equation where D_t, D_{pc}, and D_{nc} represent the absorbance of test sample, positive and negative control, respectively.

$$\mathrm{HP}(\%) = \frac{D_t - D_{nc}}{D_{pc} - D_{nc}} \times 100$$

The experiment was carried out in triplicates. The HP values categorize the biomaterials as hemolytic (over 5%), slightly hemolytic (between 2–5%) and non-hemolytic (below 2%).

2.8.2 Morphology of RBC

Effect of nanoparticles on the morphology and structural integrity of RBCs was studied by incubating the diluted RBC suspension (0.2 mL) with 100 µg/mL SPION, curcumin and Cur–SPION dispersed in PBS (0.8 mL) for a period of 2 h. The samples were fixed using 1% glutaraldehyde solution and further incubated at 37 °C for 1 h. Fixed cells were dehydrated in increasing concentrations of ethanol (50, 60 70, 80, 90, and 100%) for 20 min each. About 10 µL cell suspension was dropped onto the glass coverslips and dried in vacuum for 24 h before imaging in scanning electron microscope (VEGA 3, Tescan).

2.8.3 Capture and release of RBCs

Although the RBCs are non-adherent cells, exposure to different substrate topography may cause damage to membrane integrity of RBCs. The ability of scaffolds on maintaining RBC integrity was qualitatively assessed by capture and release of RBCs. In brief, 80 µL diluted RBC suspension was dropped on nanofibrous scaffolds and incubated for 30 min under static conditions at 37 °C. For capture, the samples were collected and fixed with 2.5% glutaraldehyde for 1 h at 37 °C. To release RBCs, samples were incubated for 30 min followed by rinsing with PBS and fixed with 2.5% glutaraldehyde for 1 h at 37 °C. After dehydration with increasing gradients of alcohol, the surface of nanofibers was visualized under FE-SEM.

2.8.4 Anticoagulant assay

The thrombo-resistant property of nanofibers was analyzed by kinetic clotting-time method. Briefly, anti-coagulated human blood (20 µL) was dropped onto the surface of nanofibers and cover slips (positive control), followed by the addition of 10 µL of $CaCl_2$ solution (0.2 mol/L) and mixed uniformly to activate blood coagulation. The samples were placed in test tubes and incubated at 37 °C for predetermined time intervals (5, 10, 20, 40 and 60 min). Finally, 5 mL of distilled water was added to the test tubes and incubated at 37 °C for 5 min before measuring the absorbance of free hemoglobin in water at 540 nm.

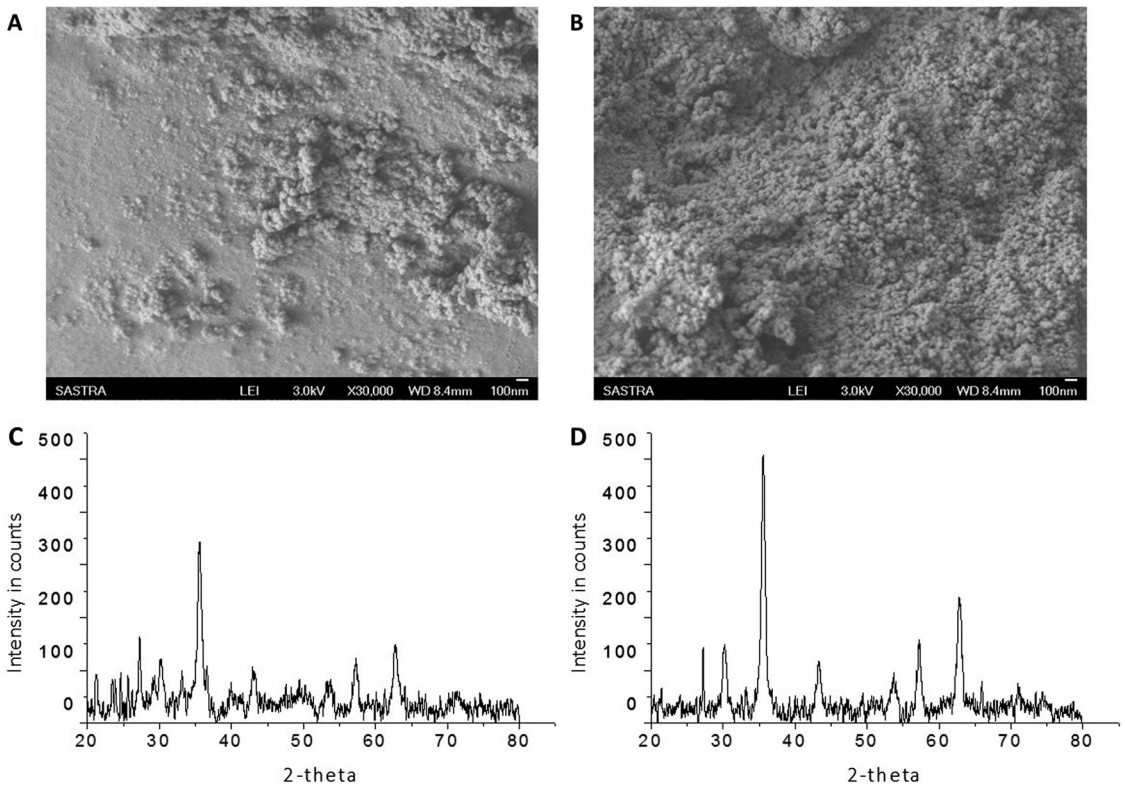

Fig. 1 Scanning Electron Micrographs of **a** SPION **b** Cur–SPION at 30,000× magnification; X-ray diffraction pattern of **c** SPION **d** Cur–SPION

2.8.5 Platelet adhesion

The effect of different topographies on platelet activation was evaluated by platelet adhesion on nanofibrous substrates and glass. Scaffolds were allowed to interact with platelet-rich plasma (PRP) collected by methods given elsewhere [26]. Substrates were placed in a sterile 24-well plate and incubated with 20 µL of PRP at 37 °C for 2 h where glass coverslip was used as positive control. The samples were carefully rinsed with PBS (pH 7.4) to remove unbound platelet. The adhered platelets were fixed with glutaraldehyde (2.5%) for 30 min and washed thrice with deionized water. The scaffolds were gradually dehydrated using graded aqueous ethanol from 50% to absolute alcohol for 15 min each. The dried and moisture-free samples were observed under FE-SEM.

2.8.6 Electrophoretic separation of adsorbed serum proteins

Blood compatibility of various nanofibrous scaffolds is determined by the serum proteins adsorbed on different topographies [27–30]. The serum proteins adsorbed on smooth, porous and Cur–SPION embedded rough nanofibrous scaffolds were investigated using sodium dodecyl sulfate–polyacrylamide gel electrophoresis (SDS–PAGE). Nanofibrous samples were immersed in PRP for allowing the proteins to adsorb for 2 h at 37 ˚C. The unbound and loosely bound proteins were removed by washing with PBS. The adsorbed proteins were eluted using sodium dodecyl sulfate (SDS). The protein samples were diluted with loading buffer, boiled up to 96 °C for 5–10 min, cooled to room temperature and loaded into the wells of casted gel (4% stacking and 10% resolving gel). Protein marker (10–250 kDa) was loaded in the first lane followed by loading the samples in subsequent lanes. Electrophoresis was performed at constant voltage (80 V) in Tris–glycine–SDS buffer using SDS–PAGE system. The gel was stained with Coomassie brilliant blue for visualizing the protein bands after electrophoretic migration of adsorbed proteins.

2.8.7 Plasma recalcification time

Plasma recalcification time (PRT) was measured to compare sample-induced delay in clotting of platelet-poor plasma (PPP) following the activation of prothrombin (factor II) in the presence of Ca^{2+}. The plasma recalcification time (PRT) reflects the delay in the intrinsic coagulation process. Platelet-poor plasma was obtained by centrifuging the whole blood at 3000 rpm for 15 min. Nanofibers and glass cover slip (positive control) were placed carefully in tubes and incubated with 0.1–0.5 mL of PPP at 37 °C for 1.5 h.

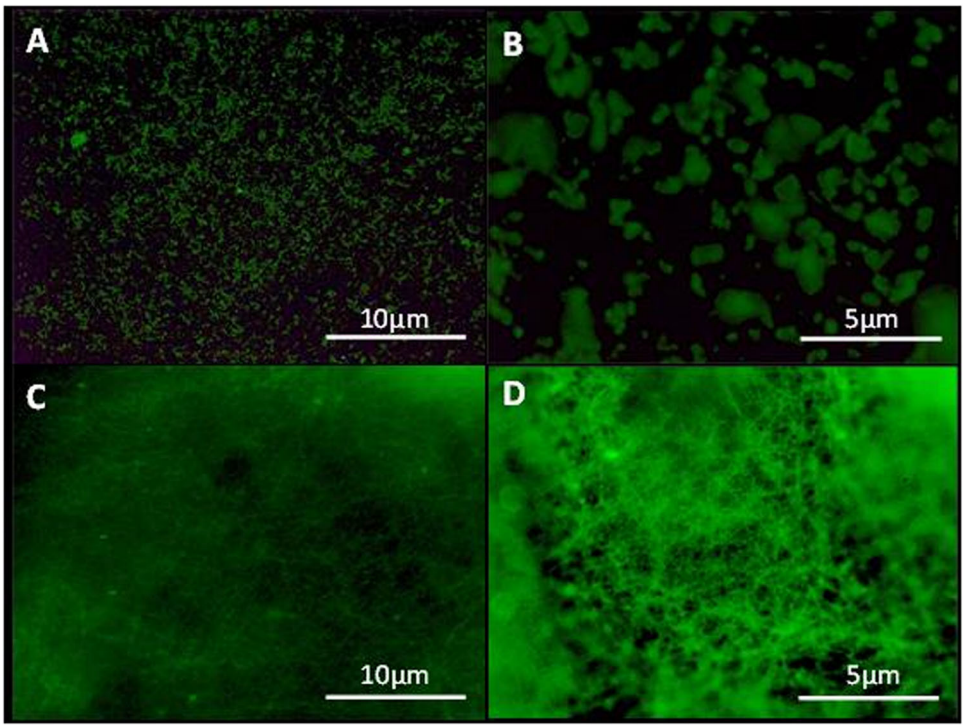

Fig. 2 Fluorescent micrographs of Cur–SPION at **a** low 4× magnification, **b** high 40× magnification, Cur–SPION embedded nanofibers (Cur–SPION NF) at **c** low 4× magnification, **d** high 40× magnification

About 0.1 mL of PPP was taken and mixed with 0.1 mL of $CaCl_2$ solution (0.025 M) in a fresh tube. The clotting time was monitored manually by dipping a stainless-steel hook into the mixture to detect fibrin threads. Clotting time was recorded at the first signs of any fibrin formation on the hook. The experiment was performed in triplicates and mean value was recorded.

2.9 Statistical analysis

All the statistical analysis was performed using Statistical Package for the social sciences, version 15.0 for Windows (SPSS v.15, US). The values were represented as mean ± standard error. Student's t-test and one-way ANOVA was performed for analyzing significant differences in value of means between groups. Further, equal variances among samples were analyzed using Tukey post-hoc test. The values were considered to be significant at $p < 0.05$.

3 Results

3.1 Physicochemical characterization of Cur–SPION

Figure 1a, b show the scanning electron micrographs of spherical SPION and Cur–SPION with an average diameter of 40.64 ± 2.05 and 45.26 ± 5.36 nm respectively prepared by one-pot synthesis. The oleic acid functionalized SPION at physiological pH showed zeta potential of –14.13 ± 1.01 mV whereas on complexation with curcumin, Cur–SPION showed a higher negative value of –20.6 ± 1.2 mV. The crystalline structure of as-synthesized SPION and Cur–SPION showed characteristic X-ray diffraction pattern and confirmed the cubic phase of γ-Fe_2O_3 at $2\theta = 35.8°$ with corresponding crystalline plane (311), that matched with JCPDS file (04-0755) (Fig. 1c, d). Further, auto-fluorescence of Cur–SPION was evident from fluorescent imaging shown in Fig. 2a, b.

3.2 Cur–SPION embedded PLA nanofibers

Synthesized Cur–SPION was embedded on PLA nanofibers in order to impart fluorescent characteristics. Figure 2c, d show the fluorescent micrographs of Cur–SPION nanofibers evidencing the subsequent incorporation of Cur–SPION all over the nanofibers. The diameter of electrospun Cur–SPION embedded PLA nanofibers was 316 ± 20 nm using scanning electron micrographs (Fig. 3e, f).

3.3 Smooth and porous PLA nanofibers

Smooth and porous topographies of nanofibers were confirmed using scanning electron micrographs. The co-solvent mixture DCM/DMF yielded smooth structures (Fig. 3a, b) while DCM/acetone solvent mixture led to the formation of heterogeneous porous nano-features on nanofibers (Fig. 3c, d). The average diameter of smooth and porous electrospun nanofibers was observed to be 308 ± 9 and 601 ± 76 nm, respectively.

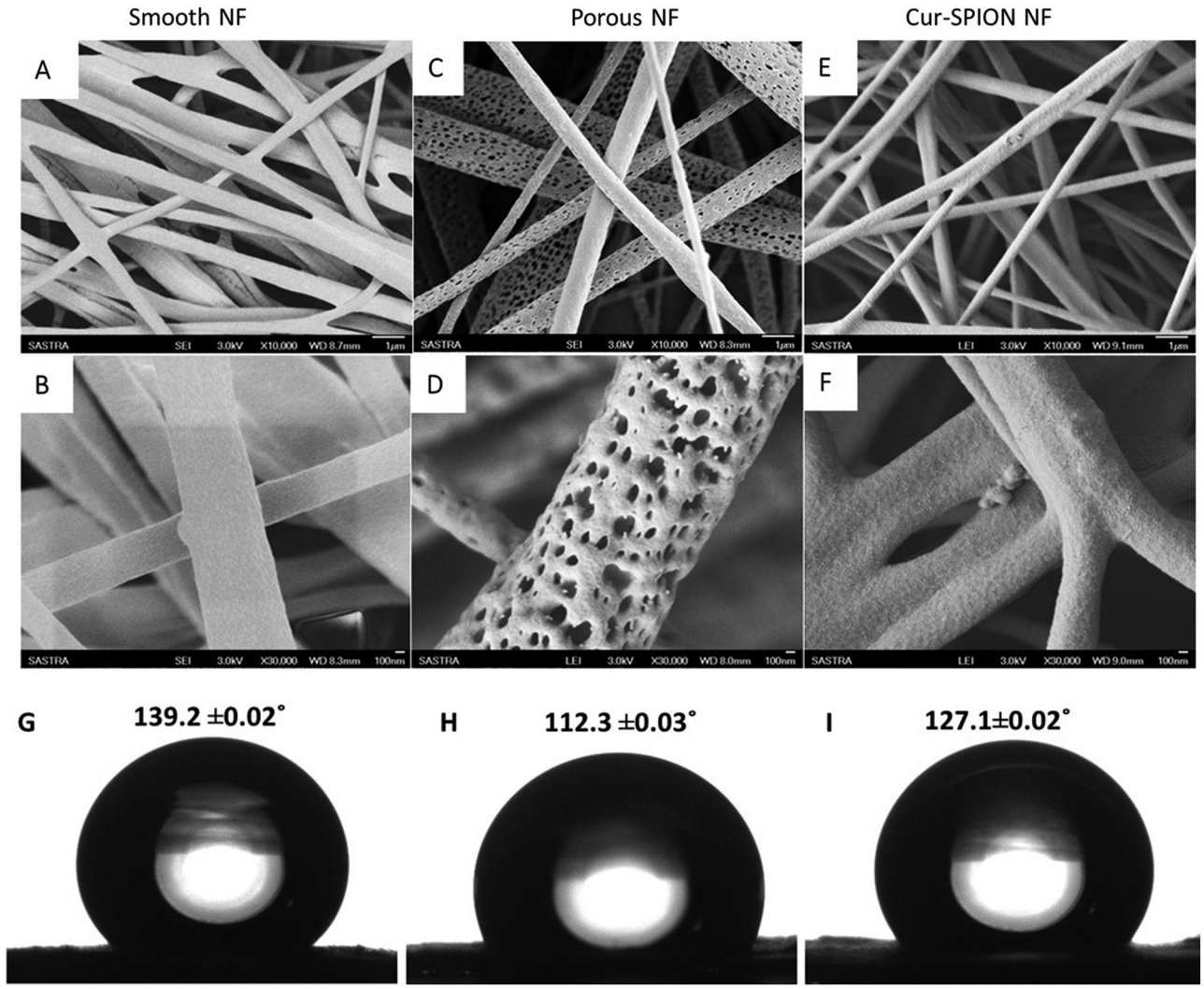

Fig. 3 Scanning electron micrographs of electrospun PLA nanofibers with different topography: **a**, **b** Smooth nanofibers, **c**, **d** porous nanofibers and **e**, **f** Cur–SPION embedded rough nanofibers at 10,000× and 30,000× magnification. Water contact angle measurements on **g** Smooth **h** porous **i** Cur–SPION nanofibers

3.4 Water contact angle

The water contact angles of smooth, porous and Cur–SPION embedded PLA nanofibers were 139.2 ± 0.02°, 112.3 ± 0.03° and 127.1 ± 0.02°, respectively (Fig. 3g–i). The contact angle was reduced in porous and Cur–SPION incorporated nanofibers when compared to smooth nanofibers.

3.5 Hemocompatibility studies

3.5.1 Hemolysis

Figure 4a shows the hemolytic percentage (HP) of both SPION and Cur–SPION at various concentrations. Although Cur–SPION showed significantly higher hemolysis at concentrations of 25 and 200 µg/mL ($p < 0.05$) compared to SPION. The HP of less than 2% in both groups clearly indicates non-hemolytic nature of nanoparticles. The hemolytic effect of smooth, porous and Cur–SPION embedded PLA nanofibers was evaluated (Fig. 4b). The HP of 1.17 ± 0.07% observed in smooth electrospun fibers confirmed that the smooth topography does not affect the integrity of RBCs thereby showing non-hemolytic nature of smooth nanofibers. On the contrary, the porous and Cur–SPION embedded rough fibers exhibited significantly higher HP of 3.80 ± 0.12% and 4.94 ± 0.06%, respectively, but lesser than the acceptable threshold value (HP > 5.00%). Membrane integrity of RBC after being exposed to Curcumin, SPION and Curcumin–SPION were evaluated by determining the morphological change using scanning electron microscopy (Fig. 4c).

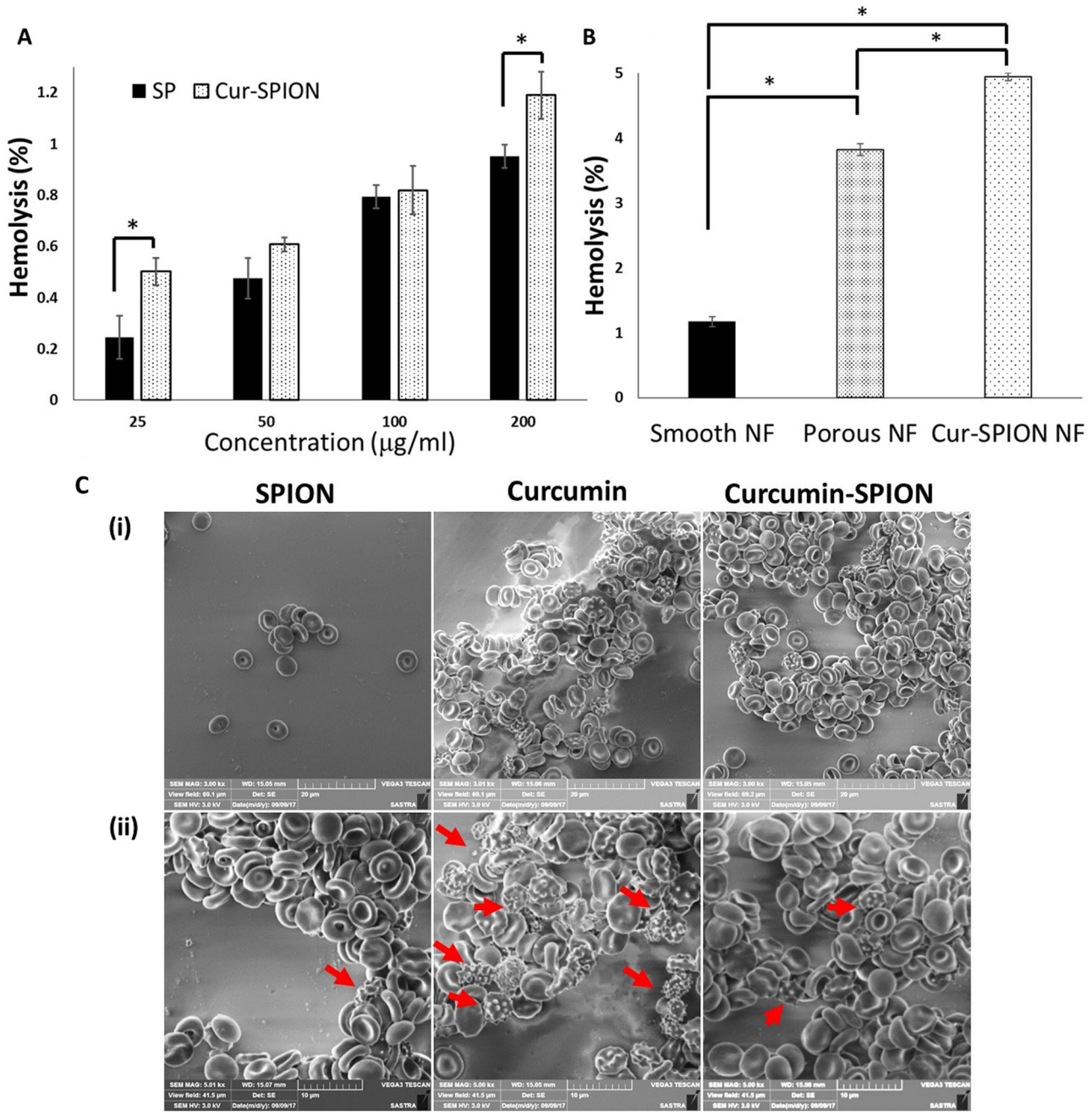

Fig. 4 **a** Hemolysis percentage of SPION and Cur–SPION; **b** Hemolysis percentage on different nanofiber topographies; **c** RBC deformation on interaction with curcumin and nanoparticles at (i) 2000× and (ii) 5000× magnification (* indicates the statistical significance between the groups $p < 0.05$)

3.5.2 Capture and release of RBCs

The efficiency to hold and gently release erythrocytes without inducing any damage was investigated further by assessing the capture and release of RBCs to substantiate the results of hemolysis (Fig. 5). More number of RBCs were retained on porous nanofibers compared to smooth fibers. Further, the adhered RBCs were found to exhibit native biconcave morphology on both porous and smooth nanofibers and released the adhered RBCs with 100% efficiency. On the contrary, Cur–SPION impregnated nanofibers did not retain many cells as smooth and porous nanofibers.

3.5.3 Plasma recalcification time

Plasma recalcification time (PRT) was calculated for the scaffolds by recording the time taken for initiation of fibrin

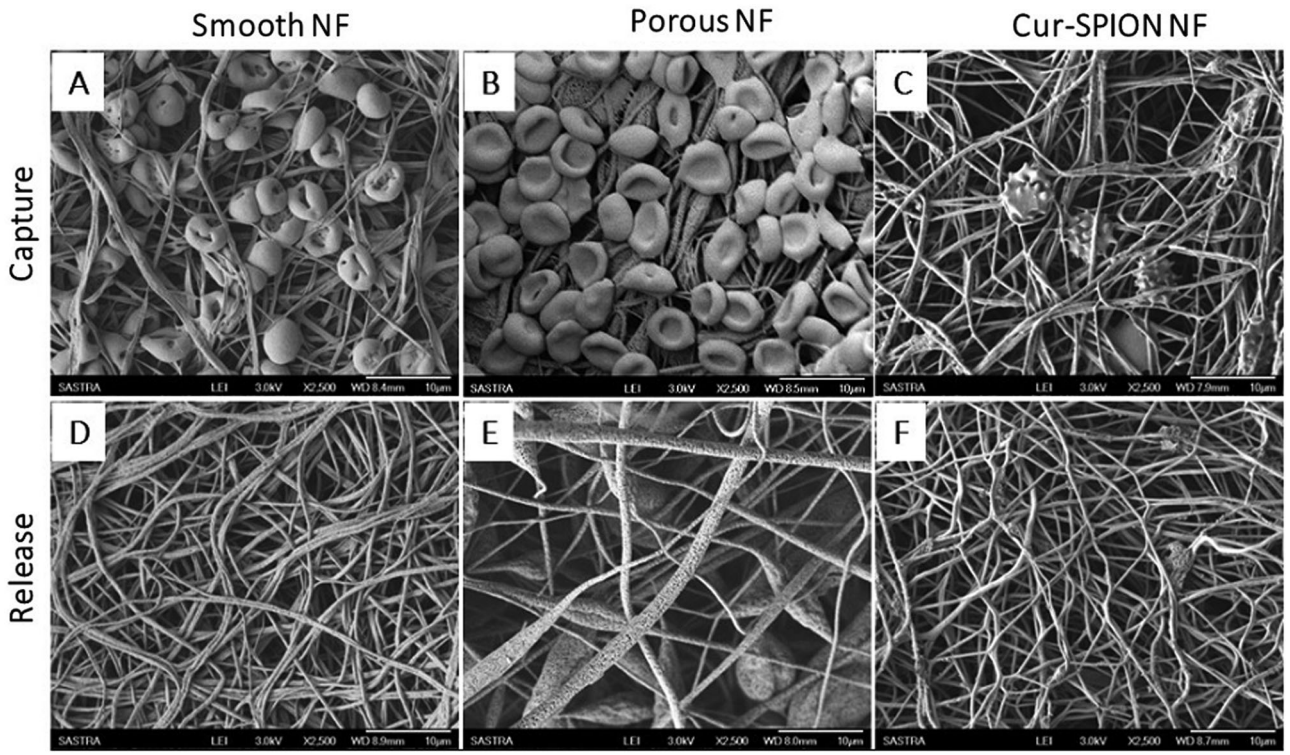

Fig. 5 Scanning electron micrographs of RBC capture and release on **a**, **d** Smooth **b**, **e** Porous **c**, **f** Cur–SPION nanofiber

thread formation. Upon contact with PPP, materials may activate the intrinsic coagulation process based on the availability of coagulation factors. Biomaterials with longer PRT exhibited better anticoagulant property. The negatively charged glass surface served as positive control as it activates the coagulation cascade by triggering adsorption of clotting proteins. Nanofibers exhibited significantly higher time for fibrin thread formation than positive control ($p < 0.05$) (Fig. 6a). Porous and Cur–SPION impregnated PLA nanofibers exhibited better anti-coagulant activity than smooth nanofibers (234 s) by showing longer and comparable clotting time of 277 and 279 s, respectively ($p > 0.05$).

3.5.4 Anticoagulant assay

The anticoagulant property of nanofibers was further evaluated by measuring free hemoglobin in the aqueous blood. After initiation of coagulation, RBCs, white blood cells (WBC) and platelets form the stabilized fibrin clot. The RBCs in the fibrin clot did not release hemoglobin and hence, measurement of free hemoglobin in the medium after exposed to nanofibers indirectly determines the anticoagulant property. Nanofibers with smooth, porous and Cur–SPION embedded fibers with rough topographies exhibited significantly higher absorbance than the glass cover slips (control, $p < 0.05$) (Fig. 6b), thereby representing higher concentration of free hemoglobin and slower rate of clotting. On the contrary, lower absorbance value in glass cover slips demonstrated faster clotting within 20 min and evidenced the thrombogenicity of glass. Among the nanofibrous substrates, porous nanofibers exhibited higher absorbance and superior anticoagulant property; whereas smooth and Cur–SPION loaded nanofibers demonstrated comparable absorbance values thereby showing negligible coagulation property.

3.5.5 Platelet adhesion

Activation of platelets was confirmed by evaluating the morphological transition of adhered platelets from discoid to fully spread appearance on nanofibers, which mainly depends on the material surface. Nanofibers with smooth topography favored platelet adhesion and exhibited fully spread morphology with no distinct pseudopodia thereby representing its positive influence on platelet activation (Fig. 7a–d). On the contrary, the porous PLA nanofibers demonstrated lesser platelet adhesion and retained discoidal morphology of platelets, which may be due to the relative hydrophilicity of nanofibrous scaffolds. Interestingly, Cur–SPION impregnated nanofibers exhibited native discoidal shape showing inactivated platelets.

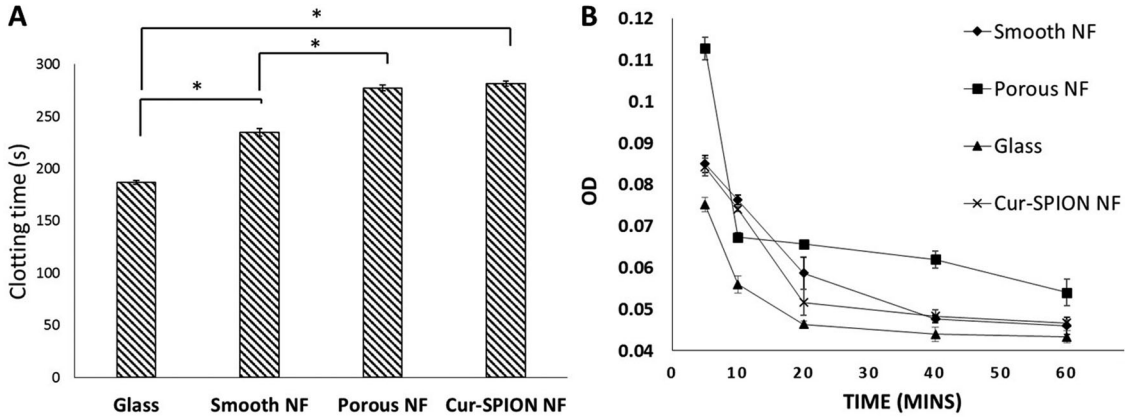

Fig. 6 **a** Plasma recalcification time of glass, smooth, porous, Cur–SPION based nanofibers; **b** Anticoagulant property of glass, smooth, porous and Cur–SPION nanofibers (*indicates the statistical significance between the groups $p < 0.05$)

3.5.6 Analysis of adsorbed serum proteins

Upon contact with blood, materials tend to adsorb specific serum proteins as primary response followed by platelet adhesion and activation of coagulation cascade resulting in thrombus formation. Hence, nanofibers with different surface topography were analyzed for serum protein adhesion using SDS–PAGE electrophoresis (Fig. 7b). Smooth nanofibers exhibited more serum proteins adsorption such as fibronectin (200–220 kDa), prothrombin (72 kDa), and albumin (66 kDa). The porous and Cur–SPION embedded rough nanofibers showed minimal protein adsorption that may be correlated with the platelet adhesion study

4 Discussion

Electrospun nanofibers with robust hemocompatibility are more promising for cardiovascular tissue engineering. Although the ECM mimetic architecture of the nanofibers favors cell adhesion and tissue progression, thrombotic events such as adsorption of serum proteins, recruitment, and activation of platelets and hemolysis majorly depends on chemical and physical nature of the scaffold surface. Immediate adsorption of proteins at the material surface followed by implantation governs the adhesion and activation of platelets that eventually enhance the thrombogenicity of scaffolds. In the present study, nanofibers with different topographies have been evaluated for the interaction of blood constituents with material surfaces to understand the hemocompatibility of various topographies. It was hypothesized that the surface topography would maintain long-lasting blood compatibility.

Despite the thorough investigation of biomaterials in vitro, many of the tissue substitutes proved to be ineffective in animal models due to the complex systemic and local responses that ultimately lead to device failure. For real-time monitoring of scaffolds with respect to individual, integration of contrast agents onto scaffolds enable the visualization of scaffolds using non-invasive techniques such as optical and MRI. However, the inclusion of contrast agents on scaffold surface may alter the chemistry, which in turn alters the blood compatibility of the scaffolds. Hence, the present study envisages the blood compatibility and interaction of various blood components on PLA electrospun scaffolds with various surface topographies such as smooth, porous and with contrasting agent (Cur–SPION). Physicochemical characterization of Cur–SPION showed increase in diameter compared to SPION which could be attributed to the hydrophobic interactions and hydrogen-bonding mediated complexation of curcumin and SPION. Hydrophobic interactions may occur between the phenyl groups of curcumin and long fatty acid chain capped SPION. The negative zeta potential value of oleic acid capped SPION can be correlated to the carboxyl groups of oleic acid and a higher negative value of Cur–SPION attributed to the increased chemical functionality of β-diketone moieties exhibiting keto–enol tautomerism in curcumin [16]. Unaltered XRD pattern of SPION in Cur–SPION confirms the purity of SPION after complexation, however the crystallinity of characteristic peak was increased. Fluorescent images of Cur–SPION PLA nanofibers evidenced the homogenous distribution of Cur–SPION all over the nanofibers this led to a rough topography was observed under SEM which may be due to the embedding of nanoparticles over the nanofibers. Porous nano-features on PLA nanofibers were observed due to the phase separation of polymer solution in DCM/acetone co-solvent mixture into polymer rich and polymer lean phases that in turn forms matrix and porous region respectively due to spontaneous vaporization of solvents [31, 32] whereas DCM/DMF co-solvent mixture yielded smooth surfaces.

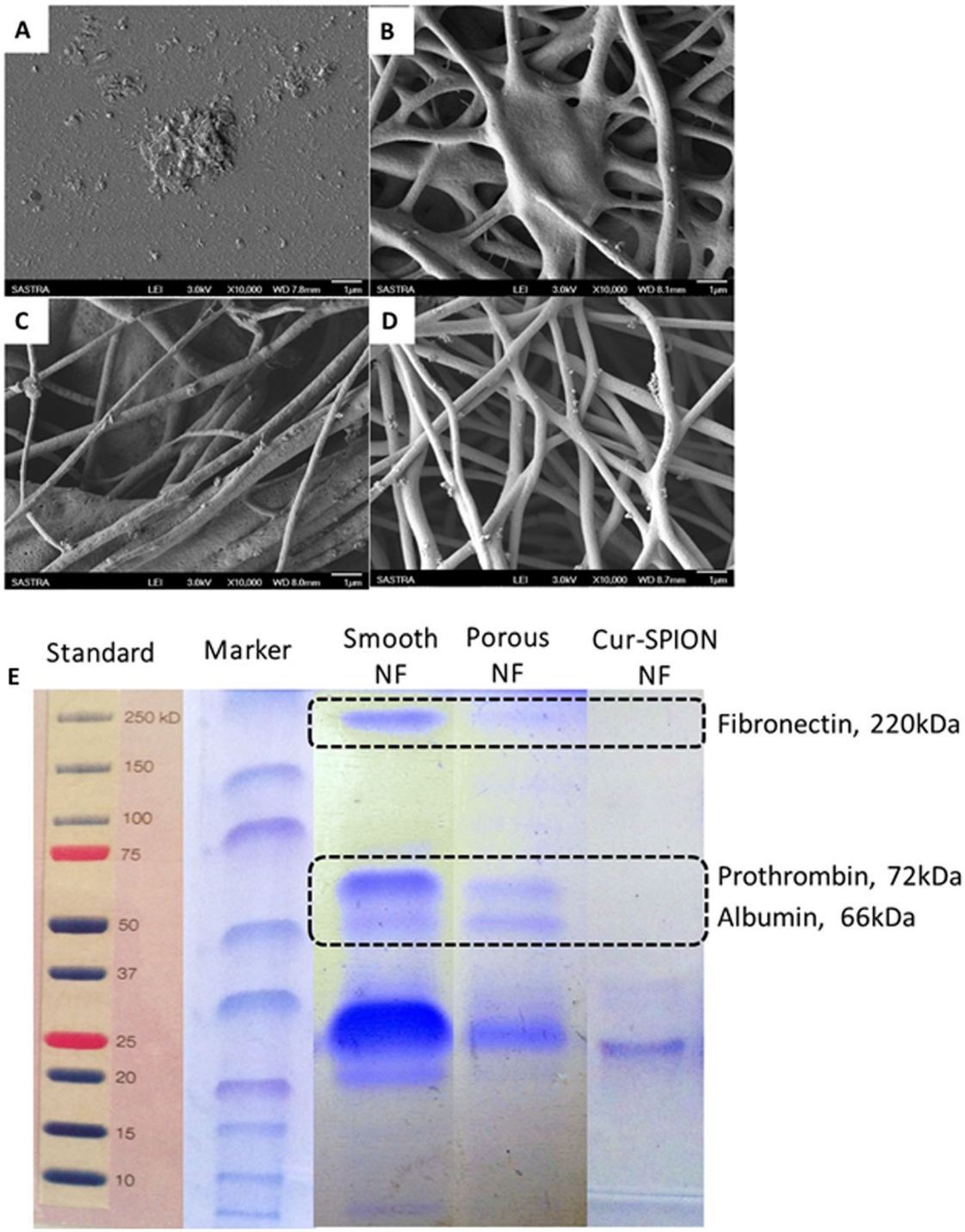

Fig. 7 Scanning electron micrographs of platelet adhesion on **a** glass, **b** smooth nanofiber **c** porous nanofiber **d** Cur–SPION nanofibers; **e** electrophoretic separation of adsorbed serum protein on various substrates by SDS–PAGE and Coomassie blue staining

These porous structures led to reduced contact angle values which may be attributed that the existence of unequal surfaces and similar pattern was obtained in Cur–SPION incorporated nanofibers due to the distribution of nanoparticles imparting both roughness and hydrophobicity to scaffold surface. The wettable property of scaffold plays a crucial role on the protein adsorption that indirectly determines the hemocompatibility of scaffolds [33, 34]. Porous, smooth and Cur–SPION nanofibers showed hemolytic values lesser than the acceptable threshold value (HP > 5%). Minimal hemolysis on porous scaffolds may be ascribed to the fragility of RBCs while contacting rougher surfaces.

Increase in HP of Cur–SPION impregnated nanofibers may be attributed to the synergistic effect of both surface chemistry (Cur–SPION) and topography (rough) on hemolysis. Similar reports were observed by Meng et al. where increase in the concentration of multiwall carbon nanotubes (MWCNT) in poly(ε-caprolactone)/MWCNTs nanofibers lead to increase in hemolysis percentage, due to shear stress that very well coincides with the above results [32]. Further, morphological changes in RBC after nanoparticle exposure was confirmed using scanning electron microscopy. Discoidal morphology of RBC was maintained in the presence of SPION whereas the morphology of fewer numbers of RBCs was altered in the presence of Curcumin–SPION and Curcumin alone. It was found that on treatment with Curcumin, RBC morphology slowly transformed to irregular shape with well-defined spicules on membrane and demonstrated the existence of both Stage I and II echinocytes. However, RBC exposed to Cur–SPION showed relatively lesser echinocyte formation (Stage I) in which Stage II echinocyte was completely absent. Curcumin being pro-oxidant, alter the membrane potential, inositol phospholipids hierarchy and calcium–calmodulin-controlled kinase activity in RBC leading to apoptosis via cell shrinkage, lipid oxidation, energy depletion and loss in transmembrane lipid asymmetry [33, 34]. The adhered RBCs on Cur–SPION based fibers undergo transformation from biconcave discocytes to echinocytes with cube-like protrusions that can be correlated with morphological transformation observed in bare curcumin and Cur–SPION treated RBCs. Capture and release assay showed higher number of RBCs trapped on porous than smooth nanofibers and exhibited native biconcave morphology. But RBCs adhered on Cur–SPION based fibers undergo transformation from biconcave discocytes to echinocytes with cube-like protrusions that can be correlated with morphological transformation observed in bare curcumin and Cur–SPION treated RBCs. This can be correlated with slight increase in the HP value ($4.94 \pm 0.06\%$) for Curcumin–SPION embedded nanofibers due to the echinocyte formation. Though better anticoagulant property was exhibited by porous and Cur–SPION loaded nanofibers than smooth nanofibers. Similar results were obtained for porous nanofibers in anticoagulant assay performed by indirect method which proved the least thrombogenic among the different topographies of nanofibers. Thrombogenicity was also determined by evaluating the extent of platelet activation on various nanofibrous scaffolds. Hydrophobic smooth nanofibers demonstrated fully extended platelet morphology and enhanced platelet activation that directly influences the adhesion of serum proteins (Fig. 3g) [35]. The hydrophilic porous nanofibers did not affect the RBC membrane integrity and did not elicit any detrimental effects on both RBC and platelets which would promote the RBC–platelet interaction and subsequently reduce RBC deformation [26]. The existence of inactivated form of platelets on the curcumin–SPION impregnated nanofibers may be due to the influence of surface chemistry, as curcumin preferentially inhibits the platelet-activating factor and arachidonic acid-mediated platelet aggregation [36]. Adsorption of plasma proteins such as fibronectin, fibrinogen, vitronectin on material surface plays a crucial role in the activation of platelets through GPIIb/IIIa receptor–mediated adhesion. SDS PAGE analysis of smooth nanofibers exhibited more serum proteins that can be correlated with the increased platelet adhesion and activation. [37]. Lesser protein adsorption properties of porous nanofibers and Cur–SPION nanofibers further authenticates the anti-thrombogenic property with the minimal hemolysis.[38]

In summary, porous, smooth and nanoparticle embedded nanofibers exhibited divergent blood-material interactions albeit the same biomaterial used for fabrication of nanofibers. Also, surface chemistry between the material and blood cells further unveil the potential effects of incorporating nano dimensions over the material surface. Therefore, this study provides insights on inducing nano-topographical features that would repress the plausible failures of cardiovascular grafts. Such variation in topographies pursue unique blood properties which can be explored further for various biomedical devices.

5 Conclusions

Electrospun PLA nanofibers with smooth and porous topographies were developed by varying the co-solvent composition. Fluorescent SPION were prepared by complexation of auto-fluorescent curcumin with SPION (Cur–SPION) and were embedded in PLA nanofibers resulting in the development of fluorescent nanofibers with rougher topography. The hemocompatibility of smooth, porous and Cur–SPION embedded rough PLA nanofibers has been investigated. Smooth nanofibers were observed to be non-hemolytic compared to porous and Cur–SPION based fibers, which are slightly hemolytic. RBCs captured on Cur–SPION integrated PLA nanofibers transformed into echinocytes with sharp protrusions, which may be due to the existence of curcumin that disturbs the RBC membrane integrity. On the contrary, smooth nanofibers demonstrated platelet extension by hydrophobicity induced serum protein adsorption whereas the Cur–SPION based nanofibers retain the discoidal shape of the platelets. Interestingly, the PLA nanofibers with porous topography did not facilitate the platelet adhesion and activation as the relative hydrophilicity detains the serum protein adsorption while demonstrating excellent anti-thrombogenicity and negligible hemolysis. Nanofibers with porous topography is a

promising material for cardiovascular applications since they exhibit time-independent activity and do not influence the morphology of platelets and RBC membrane integrity while showing superior anti-thrombogenic property.

Acknowledgements The authors wish to acknowledge SASTRA Deemed University for infrastructural support and all the funding agencies for their financial support.

Author's contributions AS and JR optimized smooth and porous nanofibers. JMR, AM and SK developed Cur–SPION and Cur–SPION nanofibers. RD performed analysis and wrote the manuscript. SS and AS conceived and designed experiments.

Funding Authors are thankful to Nano Mission (SR/NM/PG-04/2015) and the FIST program (SR/FST/ST/LSI-453/2010) of the Department of Science & Technology (DST), Government of India for their financial support. One of the authors JR is thankful to Innovation in Science Pursuit for Inspired Research (INSPIRE), DST, India for Senior Research Fellowship (IF120692).

Compliance with ethical standards

Conflict of interest The authors declare that they have no conflict of interest.

References

1. Nag T, Ghosh A. Cardiovascular disease risk factors in Asian Indian population: a systematic review. J Cardiovasc Dis Res. 2013;4:222–8.
2. Bowlin GL. The daunting quest for a small. Expert Rev Med Devices. 2005;2:647–51.
3. Gorbet MB, Sefton MV. Biomaterial-associated thrombosis: roles of coagulation factors, complement, platelets and leukocytes. Biomaterials. 2004;25:5681–703.
4. De Mel A, Cousins BG, Seifalian AM, Hampstead F. NHS Trust, P Street, L Nw, Surface modification of biomaterials : a quest for blood compatibility interactions : thrombogenicity, Int J Biomater 2012; vol. 2012, Article ID 707863, 8 pages.
5. Victoria Leszczak KCP, Smith BS. Hemocompatibility of polymeric nanostructured surfaces,. J Biomater Sci Polym Ed. 2014;24:1529–48.
6. Weber N, Wendel HP, Ziemer G. Hemocompatibility of heparin-coated surfaces and the role of selective plasma protein adsorption. Biomaterials. 2002;23:429–39.
7. Li M, Guo Y, Wei Y, Macdiarmid AG, Lelkes PI. Electrospinning polyaniline-contained gelatin nanofibers for tissue engineering applications. Biomaterials. 2006;27:2705–15.
8. Nel AE, Mädler L, Velegol D, Xia T, Hoek EMV, Somasundaran P, Klaessig F, Castranova V, Thompson M. Understanding biophysicochemical interactions at the nano–bio interface. Nat Mater. 2009;8:543–57.
9. Taylor P, Sundaramurthi D, Krishnan UM. Electrospun nanofibers as scaffolds for skin tissue engineering electrospun nanofibers as scaffolds for skin. Polym Rev. 2014;54:348–76.
10. Subramanian A, Krishnan UM, Sethuraman S. Axially aligned electrically conducting biodegradable nanofibers for neural regeneration. J Mater Sci Mater Med. 2012;23:1797–809.
11. Qi P, Maitz MF, Huang N. Surface modification of cardiovascular materials and implants. Surf Coat Technol. 2013;233:80–90.
12. Ku SH, Park CB. Human endothelial cell growth on mussel-inspired nanofiber scaffold for vascular tissue engineering. Biomaterials. 2010;31:9431–7.
13. Ren X, Feng Y, Guo J, Wang H, Li Q, Yang J, Hao X, Lv J, Ma N, Li W. Surface modification and endothelialization of biomaterials as potential scaffolds for vascular tissue engineering applications. Chem Soc Rev. 2015;44:5680–742.
14. Ji Y, Wei Y, Liu X, Wang J, Ren K, Ji J. Zwitterionic polycarboxybetaine coating functionalized with REDV peptide to improve selectivity for endothelial cells. J Biomed Mater Res Part A. 2012;100:1387–97.
15. Mo XM, Xu CY, Kotaki M, Ramakrishna S. Electrospun P(LLA-CL) nanofiber: a biomimetic extracellular matrix for smooth muscle cell and endothelial cell proliferation. Biomaterials. 2004;25:1883–90.
16. Kin K, Shan P, Fan S, Ming S, Lun K, Hee A, Chow L, Wu EX, Baum L. Curcumin-conjugated magnetic nanoparticles for detecting amyloid plaques in Alzheimer's disease mice using magnetic resonance imaging (MRI). Biomaterials. 2015;44:155–72.
17. Weissleder R, Cheng H-C, Bogdanova A, Bogdanov A. Magnetically labeled cells can be detected by MR imaging. J Magn Reson Imaging. 1997;7:258–63.
18. Zhang H, Xia J, Pang X, Zhao M, Wang B, Yang L, Wan H, Wu J, Fu S. Magnetic nanoparticle-loaded electrospun polymeric nanofibers for tissue engineering. Mater Sci Eng C. 2016;73:537–43.
19. Schaefer O, Langer M. Detection of recurrent rectal cancer with CT, MRI and PET/CT. Eur Radiol. 2007;17:2044–54.
20. Mertens ME, Frese J, Bölükbas DA, Hrdlicka L, Golombek S, Koch S, Mela P, Jockenhövel S, Kiessling F, Lammers T. FMN-coated fluorescent USPIO for cell labeling and non-invasive MR imaging in tissue engineering. Theranostics. 2014;4:1002–13.
21. Yahia-ammar A, Sierra D, Me F. Self-assembled gold nanoclusters for bright fluorescence imaging and enhanced drug delivery. ACS Nano. 2016;10:2591–9.
22. AY, Junhua Yu RMD, Choi S, Richards CI. Live cell surface labelling with fluorescent Ag nanocluster conjugates. Photochem Photobiol. 2008;84:1435–9.
23. Manigandan A, Handi V, Sundaramoorthy NS, Dhandapani R, Radhakrishnan J, Sethuraman S, Subramanian A. Responsive nanomicellar theranostic cages for metastatic breast cancer. Bioconjugate Chem. 2018;29:275–286.
24. Elahi MF, Guan G, Wang L, King MW. Improved hemocompatibility of silk fibroin fabric using layer- by-layer polyelectrolyte deposition and heparin immobilization,. J Appl Polym Sci. 2014;40772:1–12.
25. Dhandayuthapani B, Varghese SH, Aswathy RG, Yoshida Y, Maekawa T, Sakthikumar D. Evaluation of antithrombogenicity and hydrophilicity on zein-SWCNT electrospun fibrous nanocomposite scaffolds, Int J Biomater. 2012; 2012, Article ID 345029, 10 pages.
26. Shi JYQ, HOu J, Zhao C, Jin J, Li C, Wong S-C. A smart core–sheath nanofiber that captures and releases red blood cells from the blood. Nanoscale. 2015;8:2022–9.
27. Scopelliti PE, Borgonovo A, Indrieri M, Giorgetti L, Bongiorno G, Carbone R, Podestà A, Milani P. The effect of surface nanometre-scale morphology on protein adsorption. PLoS One. 2010;5:1–9.
28. Denis FA, Hanarp P, Sutherland DS, Gold J, Mustin C, Rouxhet PG, Dufrêne YF. Protein adsorption on model surfaces with controlled nanotopography and chemistry. Langmuir. 2002;18:819–28.
29. Celebioglu A, Uyar T. Electrospun porous cellulose acetate fibers from volatile solvent mixture. Mater Lett. 2011;65:2291–4.

30. Wei J, Igarashi T, Okumori N, Igarashi T, Maetani T, Liu B, Yoshinari M. Influence of surface wettability on competitive protein adsorption and initial attachment of osteoblasts. Biomed Mater. 2009;4:45002.
31. Xu LC, Siedlecki CA. Effects of surface wettability and contact time on protein adhesion to biomaterial surfaces. Biomaterials. 2007;28:3273–83.
32. Meng ZX, Zheng W, Li L, Zheng YF. Fabrication and characterization of three-dimensional nanofiber membrance of PCL – MWCNTs by electrospinning. Mater Sci Eng C. 2010;30:1014–21.
33. Storka A, Vcelar B, Klickovic U, Gouya G, Weisshaar S, Aschauer S, Helson L, Wolzt M. Effect of liposomal curcumin on red blood cells in vitro. Anticancer Res. 2013;33:3629–34.
34. Chukhlovin AB. Apoptosis and red blood cell echinocytosis: common features. Scanning Microsc. 1996;10:795–803.
35. Wang H, Lin Z, Liu X, Sheng S, Wang J. Heparin-loaded zein microsphere film and hemocompatibility. J Control Release. 2005;105:120–31.
36. Shah BH, Nawaz Z, Pertani SA, Roomi A, Mahmood H, Saeed SA, Gilani AH. Inhibitory effect of curcumin, a food spice from turmeric, on platelet-activating factor- and arachidonic acid-mediated platelet aggregation through inhibition of thromboxane formation and Ca2+ signaling. Biochem Pharmacol. 1999;58:1167–72.
37. Tsai W-B, Grunkemeier JM, Horbett TA. Human plasma fibrinogen adsorption and platelet adhesion to polystyrene. J Biomed Mater Res. 1999;44:130–9.
38. Shi JYQ, Hou J, Xu X, Gao J, Li C, Jin J, Wong S-C. Capture and release erythrocyte from the blood with thermoresponsive and core-sheath PCL/PNIPAAm nanofibers. Adv Mater Interfaces. 2016;3:1500652.